

## RESEARCH ARTICLE SUMMARY

## STRUCTURAL BIOLOGY

## Structures from intact myofibrils reveal mechanism of thin filament regulation through nebulin

Zhexin Wang<sup>†</sup>, Michael Grange<sup>†</sup>, Sabrina Pospich, Thorsten Wagner, Ay Lin Kho, Mathias Gautel, Stefan Raunser\*

**INTRODUCTION:** Muscles underpin movement and heart function. Contraction and relaxation of muscles relies on the sliding between two types of filaments—the thin filament [made up of mainly filamentous actin (F-actin), tropomyosin, and troponin] and the thick myosin filament. Additionally, several other proteins are involved in the contraction mechanism, and their mutational malfunction can lead to debilitating and even life-threatening diseases. One such component in skeletal muscle, nebulin, binds to the thin filaments and stabilizes them. It is also responsible for maintaining the length of thin filaments and is involved in regulating myosin binding. Nebulin consists mainly of tandem repeats with different sequences but a conserved SDxxYK motif. Mutations in the nebulin gene are closely linked

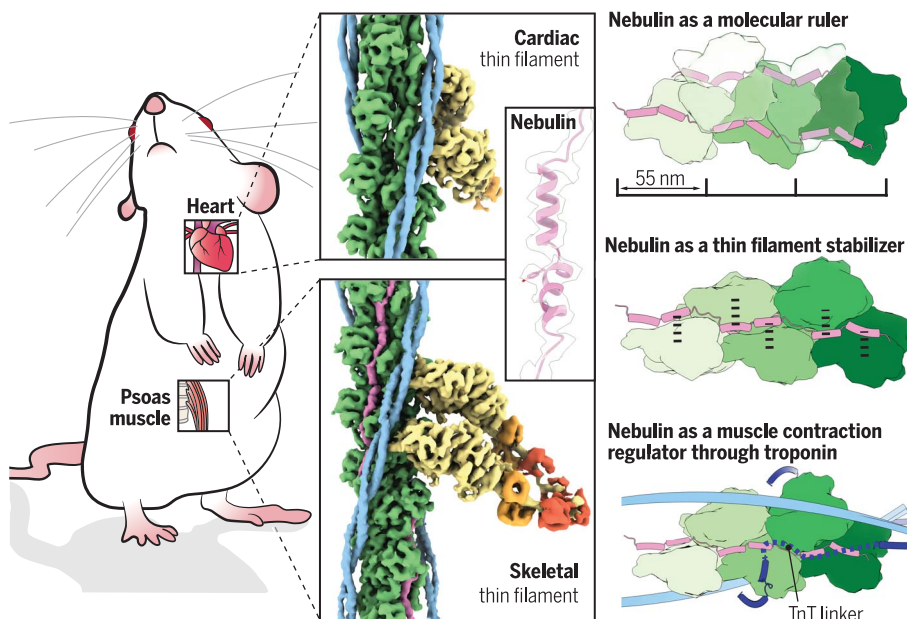
to a group of muscle diseases called nemaline myopathies.

**RATIONALE:** The mechanism underlying nebulin stabilization and the regulation of thin filaments remains nebulous because of missing structural information about the protein. It has been challenging to characterize isolated nebulin because of its enormous size and elongated and flexible nature. To investigate the structure of nebulin in its native environment, we prepared myofibrils from skeletal and cardiac muscle using focused ion beam milling and imaged them using cryo-electron tomography (cryo-ET). With subtomogram averaging, we obtained structures of cardiac and skeletal thin filaments. Because nebulin is only present in skeletal but not cardiac muscle, comparing the thin filament structures allowed

us to unambiguously identify and characterize nebulin in the native muscle.

**RESULTS:** We resolved nebulin bound to the thin filament within myofibrils isolated from the mouse psoas muscle at near-atomic resolution. In skeletal muscle, two elongated nebulin molecules bind along one actin filament. The structure reveals a 1:1 binding stoichiometry between nebulin repeats and actin subunits. Each nebulin repeat consists of two helices separated by a kink and followed by a loop region. Different nebulin repeats located at different positions along the filament have the same physical length despite their slightly varying sizes, which supports the role of nebulin as a “molecular ruler.” A nebulin repeat interacts with all three neighboring actin subunits though the SDxxYK motif and other conserved charged residues. This explains how nebulin stabilizes the thin filament. Additionally, the position of nebulin on the filament demonstrates that it does not interact with tropomyosin or myosin but likely with a troponin T (TnT) linker. Our reconstruction of myosin shows that the myosin double head exhibits inherent variability within a sarcomere and that nebulin does not alter actin-myosin interactions directly. Therefore, we propose that the myosin-binding regulatory role of nebulin is through its potential interactions with TnT. Nebulin is likely to interact with the TnT linker on two sites, which feature a WLKGIGW motif and a ExxK motif.

**CONCLUSION:** Our results show that nebulin is an integral component of the thin filament in skeletal muscle. The interactions between nebulin and other thin filament components set the molecular basis for its functions in thin filament stabilization, length control, and myosin-binding regulation. Our structure of nebulin enables the development of experimental models that further help to reveal how mutations responsible for nemaline myopathies affect nebulin's function in the sarcomere. The in situ structures of nebulin and myosin illustrated differences from in vitro characterizations and provided structural details relevant in a biology context. Our approach—using focused ion beam milling and cryo-ET to study the proteins of muscles at high resolution—paves the way for studying other muscle components in the future to understand muscle diseases at the molecular level. ■



**In situ structure of nebulin on the thin filament from mouse skeletal muscle.** Nebulin, resolved at a resolution of 4.5 Å, was identified by comparing cardiac and skeletal thin filament structures. The structure of nebulin reveals the mechanism underlying its function to maintain the length and stability of the thin filament and to regulate muscle contraction. Actin, nebulin, tropomyosin, TnT, myosin heavy chain, myosin essential light chain, and myosin regulatory light chain are colored in green, magenta, light blue, dark blue, yellow, orange, and red, respectively.

The list of author affiliations is available in the full article online.  
\*Corresponding author. Email: stefan.raunser@mpi-dortmund.mpg.de

<sup>†</sup>These authors contributed equally to this work.

Cite this article as Z. Wang *et al.*, *Science* **375**, eabn1934 (2022). DOI: 10.1126/science.abn1934

**S READ THE FULL ARTICLE AT**  
<https://doi.org/10.1126/science.abn1934>

## RESEARCH ARTICLE

## STRUCTURAL BIOLOGY

## Structures from intact myofibrils reveal mechanism of thin filament regulation through nebulin

Zhexin Wang<sup>1†</sup>, Michael Grange<sup>1‡</sup>, Sabrina Pospich<sup>1</sup>, Thorsten Wagner<sup>1</sup>, Ay Lin Kho<sup>2</sup>, Mathias Gautel<sup>2</sup>, Stefan Raunser<sup>1\*</sup>

In skeletal muscle, nebulin stabilizes and regulates the length of thin filaments, but the underlying mechanism remains nebulous. In this work, we used cryo-electron tomography and subtomogram averaging to reveal structures of native nebulin bound to thin filaments within intact sarcomeres. This in situ reconstruction provided high-resolution details of the interaction between nebulin and actin, demonstrating the stabilizing role of nebulin. Myosin bound to the thin filaments exhibited different conformations of the neck domain, highlighting its inherent structural variability in muscle. Unexpectedly, nebulin did not interact with myosin or tropomyosin, but it did interact with a troponin T linker through two potential binding motifs on nebulin, explaining its regulatory role. Our structures support the role of nebulin as a thin filament “molecular ruler” and provide a molecular basis for studying nemaline myopathies.

Nebulin is a major structural protein of skeletal sarcomeres and is essential for proper assembly and contraction of skeletal muscle (1). A sarcomere is composed of thin filaments made up of mainly filamentous actin (F-actin), tropomyosin, and troponin- and myosin-containing thick filaments. Thin and thick filaments are organized into morphologically distinct zones. The Z-disc and M-band mark the boundary and center of a sarcomere, respectively. Proximal to the Z-disc is the I-band, which contains only thin filaments. Between the M-band and the I-band, myosin cross-bridges are formed between thin and thick filaments in the A-band (fig. S1A) (2). A single nebulin molecule (with a molecular weight of >700 kDa) has been proposed to bind along the entire thin filament from the Z-disc to near the M-band (3, 4), maintaining the stability of thin filaments (5). Mutations in its encoding gene, *NEB*, are a major cause of a class of skeletal muscle disorders called nemaline myopathies that present with a range of pathological symptoms, such as hypotonia, muscle weakness, and, in some cases, respiratory failure leading to death (6–8). Despite the critical role of nebulin in skeletal muscle, nebulin is only minimally expressed in cardiac muscle (9), where instead nebulin, a short homolog of nebulin, is present but only close to the Z-disc. The absence of nebulin results in

a broader range of thin filament lengths (10) in cardiomyocytes that possibly enables greater tunability of activation (11).

Nebulin primarily consists of 22 to 28 tandem super repeats. Each super repeat consists of seven simple repeats, each made up of 31 to 38 amino acid residues, featuring a conserved sequence motif SDxxYK (12, 13). The N and C termini of nebulin associate with the capping proteins on the two ends of the thin filaments, tropomodulin (toward the M-band) (14) and CapZ (at the Z-disc) (15), respectively. Nebulin is thus hypothesized to regulate thin filament length as a molecular ruler, albeit with the exact mechanism still unknown (5, 16–19). Genetic ablation of nebulin in mice is lethal and results in sarcomeres with loss of their length regulation (20, 21).

It has been suggested that, based on the modular sequence of nebulin, each simple repeat would bind to one actin subunit, and every seventh repeat—i.e., a super repeat—would interact with the tropomyosin-troponin regulatory complex (12). However, structural details of these interactions and native nebulin are lacking. It therefore remains unclear how nebulin stabilizes or regulates thin filaments. The enormous size of nebulin combined with its elongated and flexible nature has prevented the use of in vitro reconstituted systems of nebulin and thin filaments that would resemble the native state in a sarcomere. Recombinant nebulin fragments bind to and bundle F-actin (22), which precludes a reconstitution approach for electron-microscopical structural biology. Here, we imaged nebulin directly inside mature mouse skeletal sarcomeres from isolated myofibrils using cryo-focused ion beam (cryo-FIB) milling and cryo-electron tomography (cryo-ET).

## In situ position of nebulin on thin filaments

We determined the structure of the core of the thin filament from intact myofibrils isolated from the mouse psoas muscle to 4.5-Å resolution and with actomyosin resolved to 6.6-Å resolution (figs. S1 and S2). In the core of the thin filament, two extra continuous densities were visible alongside the actin filament (Fig. 1, A to C). The elongated structure predicted for nebulin (23) suggested that this density might be natively organized nebulin bound to the thin filament. To verify this putative identification, we determined the in situ actomyosin structure in the A-band from cardiac muscle (fig. S3, A and B). Nebulin is barely expressed and is only present in small subpopulations of myofibrils in cardiac muscle. The averaged reconstruction of the cardiac thin filament, determined to an overall resolution of 7.7 Å with the core of the thin filament resolved to 6.3 Å, depicts similar organizations of actin, myosin, and tropomyosin. Notably, the extra density observed in skeletal actomyosin was missing (Fig. 1E), consistent with this density corresponding to averaged segments of nebulin.

Nebulin was observed in the grooves between the two strands of the actin filament, in accordance with their helical turn (Fig. 1A). Nebulin occupies a site that is known to be bound by actin-stabilizing compounds, such as phalloidin and jaspilakinolide (24) (fig. S4). This may explain why excessive phalloidin can unzip nebulin from thin filaments (25) and may also suggest a similar mechanism of F-actin stabilization. Like phalloidin, nebulin binding to F-actin did not alter the helical arrangement of F-actin or the conformation of the actin subunits (Fig. 2, A and B). A single actin filament was decorated by two nebulin molecules on the opposite sides (Fig. 1B). To ascertain the molecular organization of nebulin in different regions of a sarcomere, we also determined the structure of the thin filament in the skeletal muscle I-band to a resolution of 7.4 Å (fig. S3, C and D). Nebulin appeared in the I-band at the same position on the thin filament as was observed within the A-band (Fig. 1D), which indicates that nebulin spans most of the thin filament (18, 26). This suggests that nebulin maintains a structural role within the sarcomere. Notably, the position of nebulin bound to actin from native skeletal muscle is different from the three putative sites previously proposed on the outer surface of the actin filament based on reconstituted actin-nebulin fragment complexes (27). The observed differences could represent the limitations of the use of in vitro fragments of nebulin or suggest different interaction patterns during sarcomerogenesis.

The position of nebulin implies that it does not interact with tropomyosin (Fig. 1B). The subdomains 3 and 4 (SD3 and SD4) of

<sup>1</sup>Department of Structural Biochemistry, Max Planck Institute of Molecular Physiology, 44227 Dortmund, Germany.

<sup>2</sup>Randall Centre for Cell and Molecular Biophysics, School of Basic and Medical Biosciences, Kings College London BHF Centre of Research Excellence, Guy's Campus, London SE1 1UL, UK.

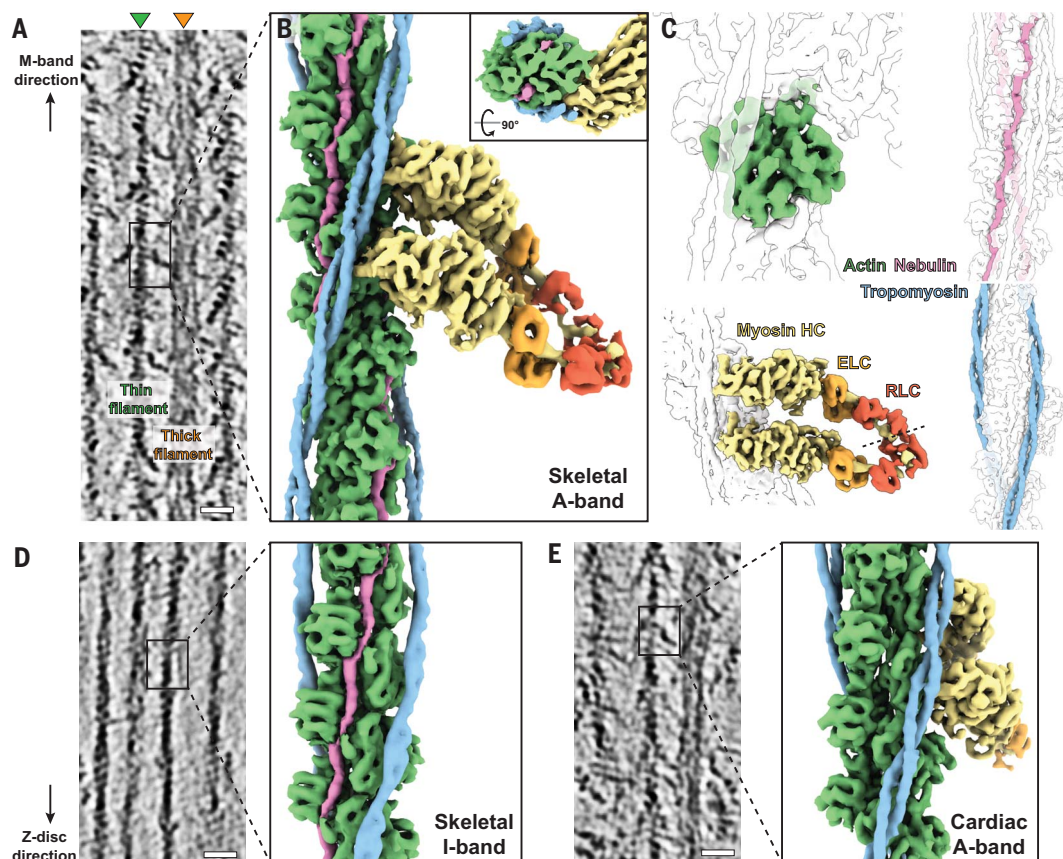
\*Corresponding author. Email: stefan.raunser@mpi-dortmund.mpg.de

†These authors contributed equally to this work. ‡Present address: Structural Biology, The Rosalind Franklin Institute, Harwell Science and Innovation Campus, Didcot OX11 0FA, UK.



**Fig. 1. Thin filament structures in striated muscle sarcomeres.**

(A) Tomographic slice of skeletal sarcomere A-band depicting adjacent thin and thick filaments. (B) Actomyosin structure from the skeletal sarcomere A-band consisting of actin (green), myosin [heavy chain (HC), yellow; essential light chain (ELC), orange; RLC, red], tropomyosin (blue), and nebulin (magenta). Myosin is a composite map including light chains from different averaged structures (see figs. S1 and S5). (Inset) Cross-sectional view of the structure. (C) Different components of a thin filament and their positions highlighted within the structure. The dotted line highlights the interface between the two RLCs of the trailing and leading myosin head. (D) Tomographic slice of a skeletal sarcomere I-band (left) and structure of the thin filament (right). (E) Tomographic slice of a cardiac sarcomere A-band (left) and structure of actomyosin, including a pair of myosin double heads (right). All tomographic slices are 7-nm thick. Scale bars, 20 nm.



adjacent actin monomers physically separate nebulin from tropomyosin, regardless of the tropomyosin state at different  $\text{Ca}^{2+}$  concentrations (28) (Fig. 2, C to F). This is contradictory to previous results from in vitro experiments (29). The discrepancy between our in situ structures and in vitro assays again demonstrates that nebulin may have different properties when purified compared with its properties in its native state in a sarcomere. Purified large fragments of nebulin are extremely insoluble when expressed (22, 30, 31). Both rotary-shadowed images of nebulin (31) and the structure of nebulin predicted by the machine learning-based software AlphaFold (32) suggest nonfilamentous structures. These visualizations clearly deviate from the elongated shape of nebulin when bound to actin filaments. Our approach of investigating nebulin inside sarcomeres therefore provides in situ structural information about nebulin interactions with the thin filament that are not accessible by sequence-based structure-prediction programs or from isolated proteins. Furthermore, during sarcomerogenesis, nebulin integration into the thin filament is likely to require cellular cofactors to prevent the formation of aggregates or large globular structures.

#### Myosin double head does not interact with nebulin and has high variability

Nebulin has been shown to regulate the actin-myosin cross-bridge cycle. It can increase thin filament activation, promote myosin binding, and thereby improve the efficiency of contraction (33–35). In vitro studies have suggested a direct interaction between a nebulin fragment and myosin (36, 37). In our rigor-state sarcomere structures, two myosin heads from a single myosin molecule are bound to the thin filament in most cross-bridges, forming a double head. However, the myosin heads do not interact with nebulin (Fig. 1A), and nebulin does not alter the interactions between actin and myosin (fig. S5B).

Having a better-resolved structure available (~9 Å in the neck domain), we were able to accurately fit the lever arms and light chains of myosin based on their secondary structure elements (fig. S5, D to F), completing the model of the entire myosin double head (Fig. 3A and fig. S5). Notably, the angles of the kinks in the lever arm helix are different between the two heads (Fig. 3A). Especially, the kink between the two regulatory light chain (RLC) lobes differs considerably in the two heads, resulting in the clamp-like arrangement of the neck domains (Fig. 3B). The RLC-

RLC interface resembles that of the RLCs of the free and blocked head in an interacting-head-motif (IHM) of an inactive myosin (38, 39), but with a rotation of ~20° (Fig. 3C). Although the motor domains are similarly arranged in the cardiac muscle (fig. S6A), our 12-Å reconstruction of the neck domain clearly demonstrates that the interface between the two RLCs is different compared with the skeletal counterpart, resulting in a subtle difference in the arrangement of the two neck domains (fig. S6B). Thus, our structures of myosin in the on state in skeletal and cardiac muscles and previous structures of myosin in the off state (38, 39) imply natural variabilities within RLCs and at the RLC-RLC interface that allow a dynamic cooperation between the two myosin heads.

We noticed that 18% of the skeletal double heads had a different conformation in which both neck domains are bent by ~20° perpendicular to the direction of the myosin power stroke (Fig. 3, D and E, and fig. S7A). This different structural arrangement increases the range within which myosin can bind to the thin filament by ~5 nm without interfering with force transmission during the power stroke (Fig. 3F). Thus, the bending contributes additional adaptability on top of that provided

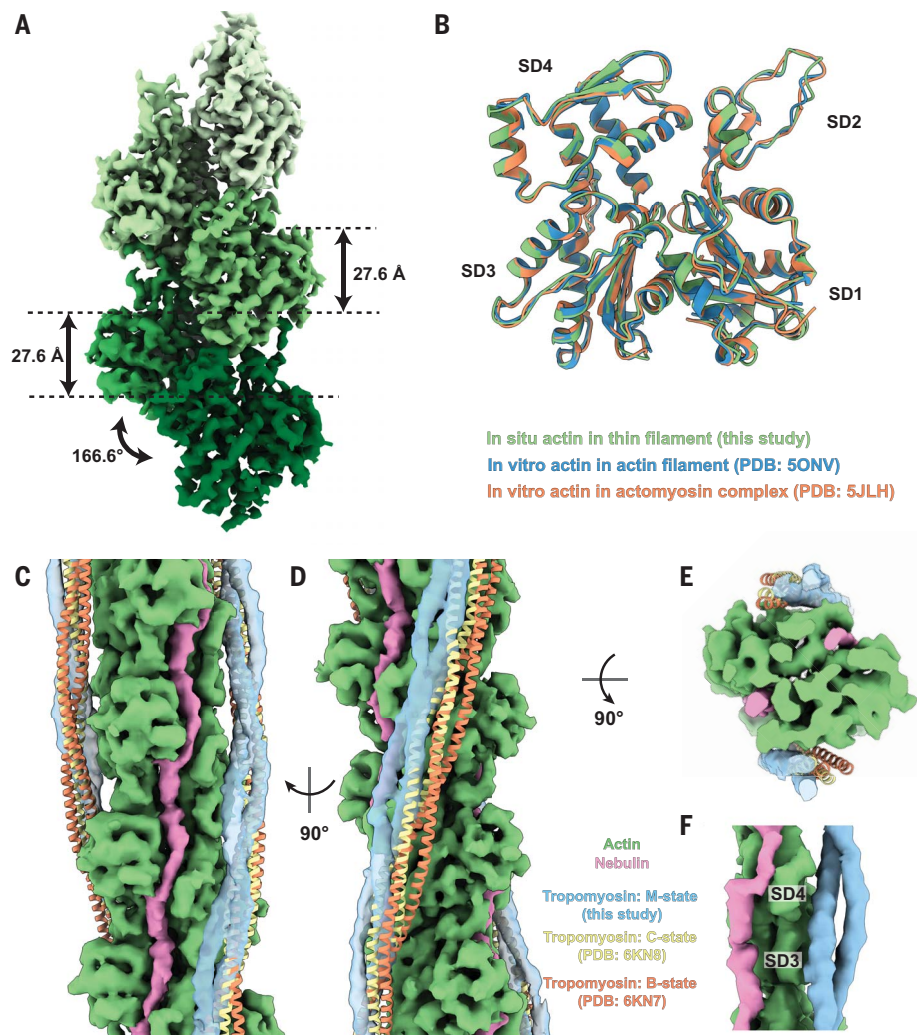


**Fig. 2. Actin in a thin filament and different tropomyosin states on a thin filament.** (A) Helical parameters of F-actin determined within a thin filament in a sarcomere. (B) Comparison of the structures of the actin subunit from different filamentous structures. (C to E) Different views depicting a thin filament, including nebulin and different states of tropomyosin. (F) Zoom-in view of nebulin, tropomyosin, and actin depicting the physical separation between nebulin and tropomyosin by the SD3 and SD4 of actin subunits.

by the flexibility of the S2 domain for cross-bridge formation between actin and myosin filaments (Fig. 3G). The myosin arm can thereby hold on tightly to a thin filament but, at the same time, have enough freedom to cooperate the mismatch between helical pitches of thick and thin filaments and account for local deformation of the sarcomere. In fact, the double heads with bent-neck domains are randomly distributed in the A-band of the sarcomere (fig. S7, B to D), ensuring efficient binding of myosin during contraction.

#### Nebulin structure and localization of residues

Although nebulin consists of repetitive simple repeats, each simple repeat has different sequences, with a few conserved charged residues and a putative actin-binding SDxxYK motif (Fig. 4, A and H, and fig. S8A). Owing to the

nature of subtomogram averaging, the obtained electron microscopy (EM) density map of nebulin is an averaged density of all repeats in the A-band. Taking advantage of the 4.5-Å map, where bulky side chains are typically resolved (fig. S2), we were able to build an atomic model for actin and refine a polyalanine nebulin model into its density (table S1). Using a published convention (12), we defined the start of a simple repeat at two residues preceding a conserved aspartic acid, resulting in the SDxxYK motif residing at positions 18 to 23.

The model of nebulin consists of a repetitive structure of two  $\alpha$  helices (H1 and H2), with a short kink of 46° in between, followed by a loop region spanning around SD1 of actin (Fig. 4, C to F). As validation, and to map the sequence to our structural model, we predicted

the average secondary structure to highlight structured and unstructured regions from the sequences of nebulin simple repeats (fig. S8B and Materials and methods). The prediction implied that each nebulin simple repeat should form a long helix, with a drop in probability in the middle of this helix (Fig. 4G). By matching the predicted start of the helix in the sequence with the start of H1 in the structure, the predicted end of the helix matched the end of H2, and the dip in probability matched the position of the kink in our model (Fig. 4, F and G). Based on this registry, a noticeable bulky side-chain density aligned with position 22, corresponding to a fully conserved tyrosine residue. We attributed this density to the phenyl group of this tyrosine (Fig. 4F and fig. S2D). This observation further validates the sequence-structure mapping. As such, H1 starts at position 5, which is often occupied by a proline (Fig. 4, F to H). The SDxxYK motif, where the exon boundaries are, is located at the beginning of H2, among which the serine is positioned at the kink between H1 and H2. This registry allowed us to assign the location of other conserved residues and further investigate their roles in the interactions between nebulin and the thin filament.

#### Nebulin as a molecular ruler of the thin filament

A molecular ruler for the actin filament should coordinate two main functions: capping of the barbed and pointed end of the filament at a defined distance and being in close association with actin subunits along the filament length. Although the general concept of nebulin as a molecular ruler is supported by its size being proportional to the length of the thin filament in different muscle fibers (16, 40), it has been speculated that the interaction of nebulin with the thin filament differs at the N and C termini (14, 15). Because we averaged over all nebulin repeats, our study does not give insights into the ends of nebulin. However, the structures of the native thin filaments clearly depict a 1:1 stoichiometry between nebulin repeats and actin subunits in both the A-band and I-band (Fig. 1D and Fig. 4D). Furthermore, unlike previously suggested (23), the repeats are distinct structural units rather than part of a contiguous  $\alpha$  helix. Thus, each nebulin repeat likely denotes the gradation of a ruler in measuring the number of actin subunits.

Although most nebulin simple repeats contain 35 amino acids (as is modeled above), some repeats can be as short as 31 amino acids or as long as 38 amino acids (fig. S8C). Different sizes of nebulin repeats typically correspond to different positions in a super repeat (Fig. 4B). The predicted secondary structure implies that, in the shorter repeats, the helix ends earlier than in an average-length repeat and, in the longer repeats, the loop is longer



**Fig. 3. Structural variability within the in situ myosin double head in skeletal muscle.**

(A) The lever arms of the trailing and leading myosin heads form kinked helices (yellow). Different angles at the kinks between the two heads are labeled. ELCs and RLCs are shown as transparent models.

(B) Different conformations of the lever arm at the RLC-binding regions of the trailing head (purple) and the leading head (green). (C) View from the eye symbol in (A) showing the interface between the RLCs from the trailing and leading head (red for RLC, yellow for lever arm helices) compared with the interface of the blocked head (aligned to the leading head) and the free head in the IHM (blue for RLC, dark blue for lever arm helices). (D) Two different conformations, straight and bent forms, of myosin double heads determined by 3D classification.

HC, ELC, and RLC regions are colored in yellow, orange, and red, respectively. (E) Comparison between the straight (orange) and bent (purple) double-head conformations. The origin of bending is marked by an asterisk, as also indicated in (A). (F) Schematic drawing describing the increased range of thin filament positions that can be bound by myosin heads because of the bending of the double heads. (G) Schematic drawing depicting the three flexible junctions in a myosin head.

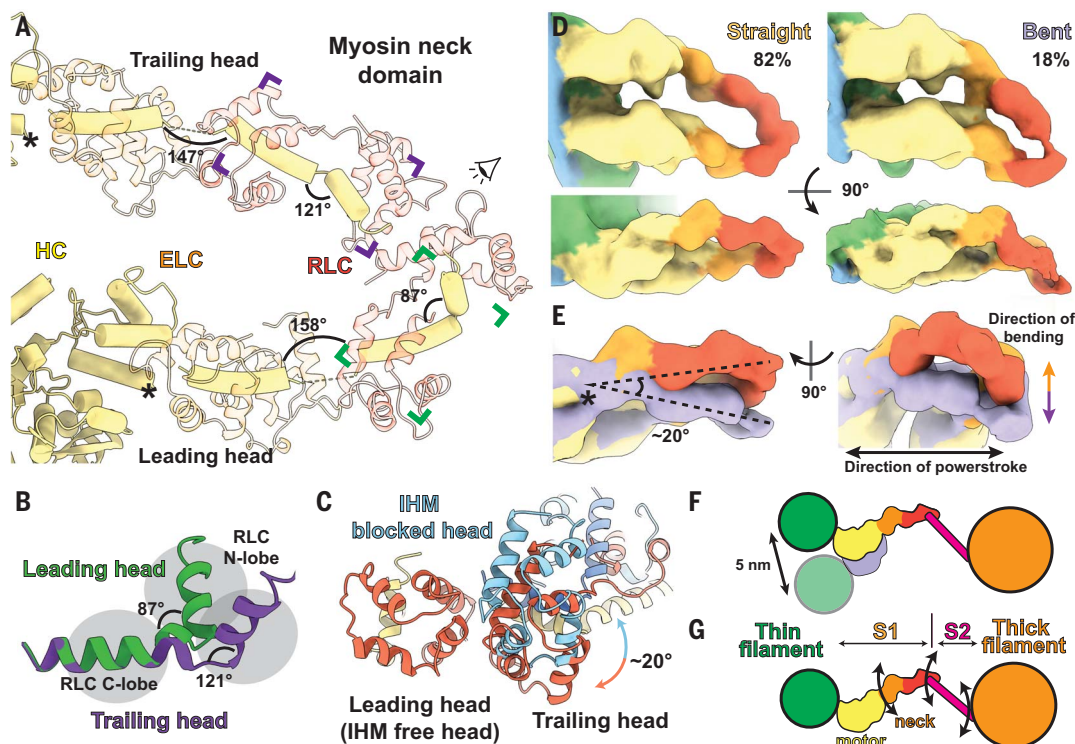


(fig. S8D). Although we did not observe separate classes within our cryo-ET data for these repeats owing to their low abundance, it is noticeable that the density corresponding to H2 and the first half of the loop has lower occupancy compared with that of H1 (fig. S8E). This suggests that in the shorter nebulin repeats, part of H2 is extruded into the loop along segments of actin to compensate for fewer amino acids, whereas in the longer nebulin repeats, the extra amino acids reside flexibly in the loop (fig. S8F). This ensures that in all regions of the sarcomere, nebulin repeats have the same physical length to span an actin subunit to maintain a 1:1 binding stoichiometry, which is one of the main functions of a molecular ruler.

### Interactions between nebulin and the thin filament

On the basis of our model, we were able to show that the interactions between actin and nebulin are mediated by residues throughout one nebulin simple repeat and three adjacent actin subunits (Fig. 5A). In the SDxxYK motif, Y22 forms a potential cation- $\pi$  interaction with K68 on SD1 of one actin subunit (N) (Fig. 5C). S18 likely forms a hydrogen bond with E276 on SD3 of the laterally adjacent actin subunit on the other strand (N+1). D19 and K23 interact with residues on SD1 and

SD2 of actin subunit N through electrostatic attractions. Additionally, other highly conserved charged residues outside the SDxxYK motif are also involved in the interactions between actin and nebulin. D3, K11, and K30 can form electrostatic interactions with SD1 of actin subunit N+2, SD4 of actin subunit N+1, and SD1 of actin subunit N, respectively (Fig. 5C). Every nebulin repeat interacts with all three neighboring actin subunits (Fig. 5A), which prevents them from depolymerizing and confers rigidity and mechanical stability to the thin filament.

An intramolecular interaction occurs between positions 15 and 21 on nebulin at the position of the kink between H1 and H2 (Fig. 5, A and B). Although both positions can accommodate either positively or negatively charged residues, they appear to be often complementary to each other among all repeat sequences (fig. S9, A to C). Their interaction is also supported by weak side-chain densities in our averaged reconstruction (fig. S9D). This intramolecular interaction stabilizes the kink conformation of the two helices, which is necessary for positioning charged residues near actin.

Nebulin simple repeats share a higher sequence similarity with the repeats that are six repeats apart, forming a seven-repeat super repeat pattern (Fig. 4B). This modular structure

suggests an interaction with the troponin-tropomyosin regulatory complex, which also has a 1:7 stoichiometry ratio to actin. The physical separation of nebulin and tropomyosin by actin has ruled out their interaction. The core of troponin, including troponin C (TnC), troponin I (TnI), and most of troponin T (TnT), is also located away from nebulin (Fig. 6A). However, a linker region in TnT between R134 and R179 is likely to be the binding partner of nebulin (Fig. 6C). It was hypothesized to cross the groove between two actin strands (41). Although nebulin and this TnT linker could not be resolved in a structure of the thin filament containing troponin determined from our data (fig. S10), previous structures of troponin with actin reported from cardiac thin filaments (42, 43) show that this TnT linker is localized close to the region where nebulin resides in our structure. Despite the lack of a structural model for the linker owing to its flexibility, superimposing previous EM densities for TnT with our structural model of actin and nebulin suggests the location of two contact sites between TnT and nebulin (Fig. 6, A and B). One site is located at the end of H2 (Fig. 6, A to C, site I). This site is consistent with the position of a WLKGIGW motif in nebulin, which has previously been proposed to be the tropomyosin-troponin binding motif at the

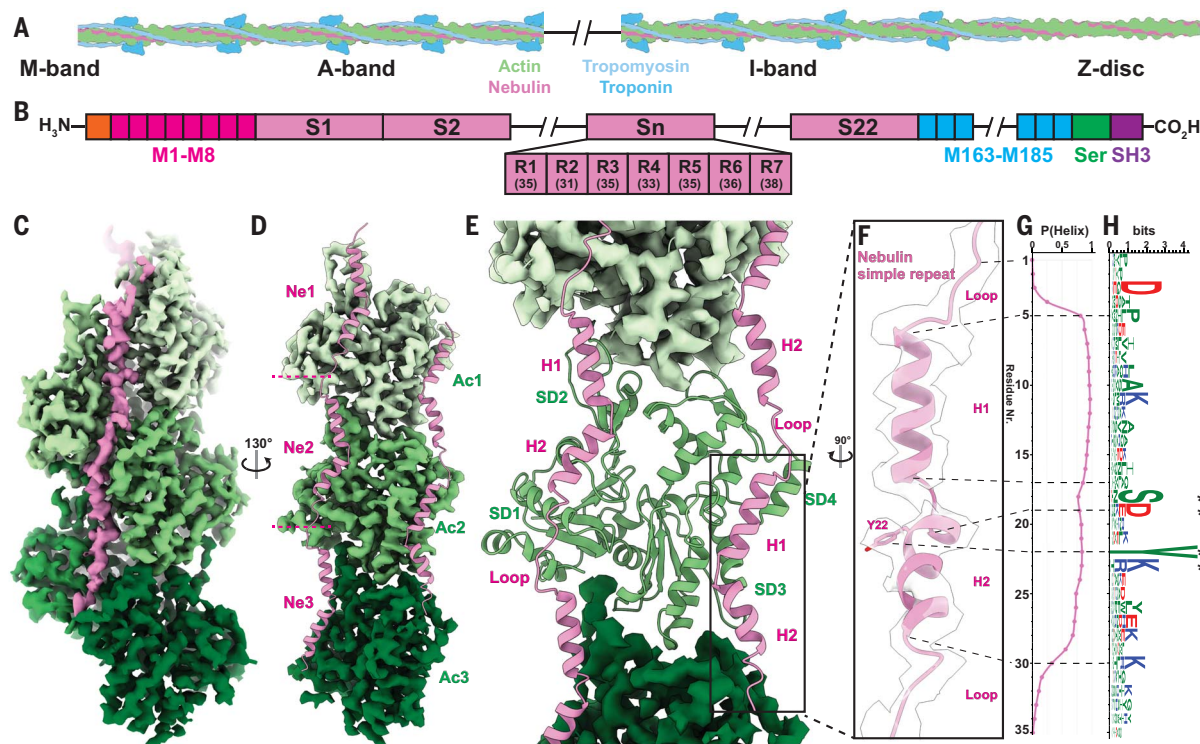


**Fig. 4. Nebulin structure and its binding to the actin filament.** (A) Schematic drawing of the nebulin-bound thin filament. (B) Modular organization of the primary sequence of nebulin demonstrating its super repeats and simple repeats. Nebulin contains an N-terminal sequence (orange), repeats 1 to 8 (M1 to M8; bright magenta), a super repeat region (magenta), repeats 163 to 185 (M163 to M185; blue), a serine-rich region (Ser; green), and a C-terminal Src homology-3 domain (SH3; purple). The number below each simple repeat indicates its most common size in number of amino acids. (C) Subtomogram-averaged structure of the actin filament in complex with nebulin (magenta) at a resolution of 4.5 Å. Different actin subunits are colored in different shades of green with darker green toward the barbed end. (D) Rotated view of (C) highlighting both nebulin (Ne) molecules (shown as structural models of three and two simple repeats) on the actin (Ac) filament. Only one strand of

the actin filament is shown. Nebulin simple repeats are labeled on one strand to show 1:1 stoichiometry with actin subunits. (E) Structural model of one actin subunit and two nebulin molecules. One nebulin binds along actin subdomains 1 and 2 (SD1 and SD2), and the other binds along actin SD3 and SD4. The averaged cryo-ET map of the neighboring actin subunits is shown. (F) Zoom-in view of one nebulin simple repeat. The side chain of residue Y22 is highlighted. (G) Averaged predicted score for an  $\alpha$  helix at each residue position of a simple repeat. (H) Graphical representation of sequence alignment of all simple repeats (M1 to M163). A larger amino acid symbol corresponds to a greater occurrence at a certain position. Positive, negative, and neutral residues are colored in blue, red, and green, respectively. Dotted lines map the sequence to the structural model in (F) and (G). Asterisks mark the conserved SDxxYK motif.

end of repeat 3 (12). The other site is located downstream of the first site at the start of H1, indicating another potential troponin-binding motif, ExxK, at the beginning of repeat 4 (Fig. 6, A to C, site II). The TnT linker region contains a hydrophobic C terminus and a highly charged N terminus matching the orientation of the two binding sites, which suggests that the WLKGIGW motif and the ExxK motif interact with TnT through hydrophobic and electrostatic interactions, respectively (Fig. 6D).

Although missense mutations have not been localized to this linker, TnT is the only troponin component where mutations can lead to nemaline myopathy (7). For example, Amish nemaline myopathy, a severe type, is caused by a *TNNT1* (slow muscle troponin) truncation (44), and a splicing variant of *TNNT3* (fast muscle troponin) can also lead to nemaline myopathy (45). This is in agreement with our

proposed interactions between nebulin and TnT. On the basis of our observation that nebulin does not interact with myosin or tropomyosin, the role nebulin plays in regulating myosin binding is likely to be a downstream effect of its interaction with the TnT linker. This interaction in skeletal muscle may rigidify the linker and thereby help to maintain efficient calcium regulation and subsequent binding of myosin. It can also increase the cooperativity in calcium regulation across the two actin strands, which has been recently observed in cardiac muscle (43).

#### Human nebulin and insights into nemaline myopathy

Nebulin in mice shares >90% sequence similarity with human nebulin (46). Key residues involved in the interactions between nebulin and the thin filament are conserved among repeats of mouse and human nebulin (fig. S11).

Our structural model of nebulin derived from mice is therefore also applicable to humans and enables the understanding of the mechanism underlying the pathogenicity caused by recessive mutations in the *NEB* gene, which is the major cause of nemaline myopathies (7). Nemaline myopathy mutations are usually compound heterozygous, in some cases with one truncating and one missense variant (7). Two missense *NEB* mutations, S6366→I (S6366I) and T7382P, have been identified as founder mutations in the Finnish population (47). The locations of the two sites on a simple repeat correspond to S18 and T14 (fig. S9E). A mutation of S18 into a hydrophobic isoleucine would disrupt its potential hydrogen bond with actin (Fig. 5C and fig. S9F). A mutation of T14 to proline, despite not being at a conserved residue position, can lead to the disruption of H1 helical secondary structure and thus alter the local conformation



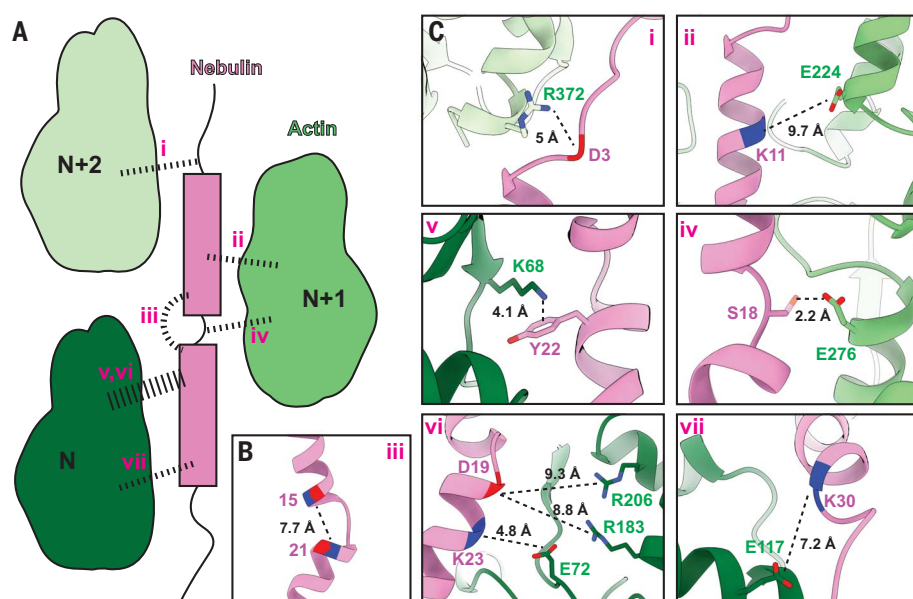


**Fig. 5. Interactions between nebulin and actin.** (A) Schematic depiction of interactions between nebulin (magenta) and three adjacent actin (green) subunits. Interactions are marked as dotted lines and labeled as i to vii. (B) Intranebulin interactions [iii in (A)] between residues with complementary charges at positions 15 and 21. (C) Details of interactions i, ii, and iv to vii in (A). Distances were measured between actin residues and the C $\beta$  of the polyalanine model of nebulin where the side chain is not resolved. A potential side-chain conformation of S18 is shown for visualization, although it was not determined from the map. Single-letter abbreviations for the amino acid residues are as follows: A, Ala; C, Cys; D, Asp; E, Glu; F, Phe; G, Gly; H, His; I, Ile; K, Lys; L, Leu; M, Met; N, Asn; P, Pro; Q, Gln; R, Arg; S, Ser; T, Thr; V, Val; W, Trp; and Y, Tyr.

of nebulin and interfere with actin binding (fig. S9F).

Our structural model of actin and nebulin maps residues crucial to maintaining the interactions between nebulin and the thin filament. When also applied to clinical genetics, this information should help to determine additional pathogenic interfaces of nebulin variants. This is especially crucial when considering missense variants, where pathogenicity is often difficult to determine (47), and will thus aid the early diagnosis of nemaline myopathies and genetic counseling of variant carriers.

## Conclusions

Our structural reconstruction of nebulin within a native skeletal sarcomere provides the basis of interaction between nebulin and thin filaments. Our structures determined across several tissue types and regions enable a comparative analysis of nebulin in its native context. This analysis reveals the mechanism underlying the roles nebulin plays in regulating thin filament length, as a thin filament stabilizer, and in regulating myosin binding through its interaction with TnT. Our approach using cryo-FIB milling and cryo-ET provides a high-resolution structural approach within an isolated tissue. Our findings highlight different conformations of myosin and illustrate similarities and differences from in vitro structures. Together with

a recent study reporting the high-resolution structure of bacterial ribosomes (48), our structures showcase the full potential of in situ structural biology using cryo-ET. In the context of the sarcomere, where several flexible proteins—such as titin and myosin-binding protein-C—are present and still lack structural visualization, our approach is a general tool for structural analysis where other methods are limited. Determining the structure of these key players in the context of native sarcomeres will enable better modeling of skeletal muscle in the future, directly affecting the understanding of disease. The structure of nebulin presented here is one such case, where the molecular interactions described might help to establish a foundation for future developments of the treatment of nemaline myopathies.

## Materials and methods

### Myofibril isolation

Skeletal myofibrils were prepared from pre-stretched BALB/c mouse psoas muscle fiber bundles, as described previously (2).

Cardiac myofibrils were prepared from left ventricular strips prestretched overnight to a sarcomere length of  $\sim 2.2 \mu\text{m}$  in rigor buffer [20 mM HEPES pH 7, 140 mM KCl, 2 mM  $\text{MgCl}_2$ , 2 mM EGTA, 1 mM dithiothreitol (DTT), Roche complete protease inhibitor] at  $4^\circ\text{C}$ . Left ventricles were cut into  $\sim 1\text{-mm}$  pieces using scalpel blades and homogenized first in

rigor buffer with complete protease inhibitors, then resuspended and homogenized three to four times in rigor buffer containing 1% (v/v) Triton X-100 essentially as described (49). Dissociation into myofibril bundles containing three to five myofibrils was monitored by microscopy. The concentration of myofibrils was adjusted with complete rigor buffer to  $\sim 5 \text{ mg ml}^{-1}$ , using an extinction coefficient of myofibrils in 1% (w/v) warm SDS solution of  $\sim 0.7 \text{ ml mg}^{-1} \text{ cm}^{-1}$ . Both cardiac myofibrils and skeletal myofibrils were prepared from 3-month female BALB/c mice, and myofibrils from both tissues were prepared from the same animal for each biological replicate.

### Vitrification of myofibrils and cryo-FIB milling

Myofibrils were frozen on grids by plunge-freezing using a Vitrobot. Generally,  $2 \mu\text{l}$  of myofibril suspension was applied onto the glow-discharged carbon side of Quantifoil R 1.2/1.3 Cu 200 grids. After a 60-s incubation at  $13^\circ\text{C}$ , the grids were blotted from the opposite side of the carbon layer for 15 s before plunging into liquid ethane. For the dataset aimed at determining the I-band thin filament structure, myofibrils were frozen on Quantifoil R 1/4 Au 200 grids with  $\text{SiO}_2$  film after a longer blotting time of 20 s. Frozen grids were clipped into cryo-FIB-specific AutoGrids with marks for grid orientation and a cut-out for low-angle FIB milling.

Clipped grids were transferred into an Aquilos cryo-FIB/scanning electron microscopy (SEM) dual-beam microscope (Thermo Fisher). Cryo-FIB milling was performed as previously described (2). Briefly, the grids were first sputter-coated with platinum and then coated with metalloorganic platinum through a gas-injection system. The myofibrils were thinned into lamellae in a four-step milling process with an ion beam of decreasing current from  $0.5 \mu\text{A}$  to  $50 \text{ nA}$ . For the dataset of I-band thin filaments, AutoTEM (TEM, transmission electron microscopy) was used to automatically produce lamellae with thicknesses of 50 to  $200 \text{ nm}$ . During auto-milling, an anticontamination shield replacing the original shutter was inserted to minimize contamination from water deposition (50).

### Cryo-ET data acquisition

Grids containing milled lamellae were transferred through a low-humidity glovebox (50), to avoid contamination, into a Titan Krios (Thermo Fisher) transmission electron microscope equipped with a K2 Summit or K3 camera (Gatan) and an energy filter. Projection images were acquired using SerialEM software (51). Overview images of myofibrils in lamellae were acquired at  $6300\times$  or  $8400\times$  nominal magnification to identify locations for high-magnification tilt series acquisition and serve as reference images for batch tomography data

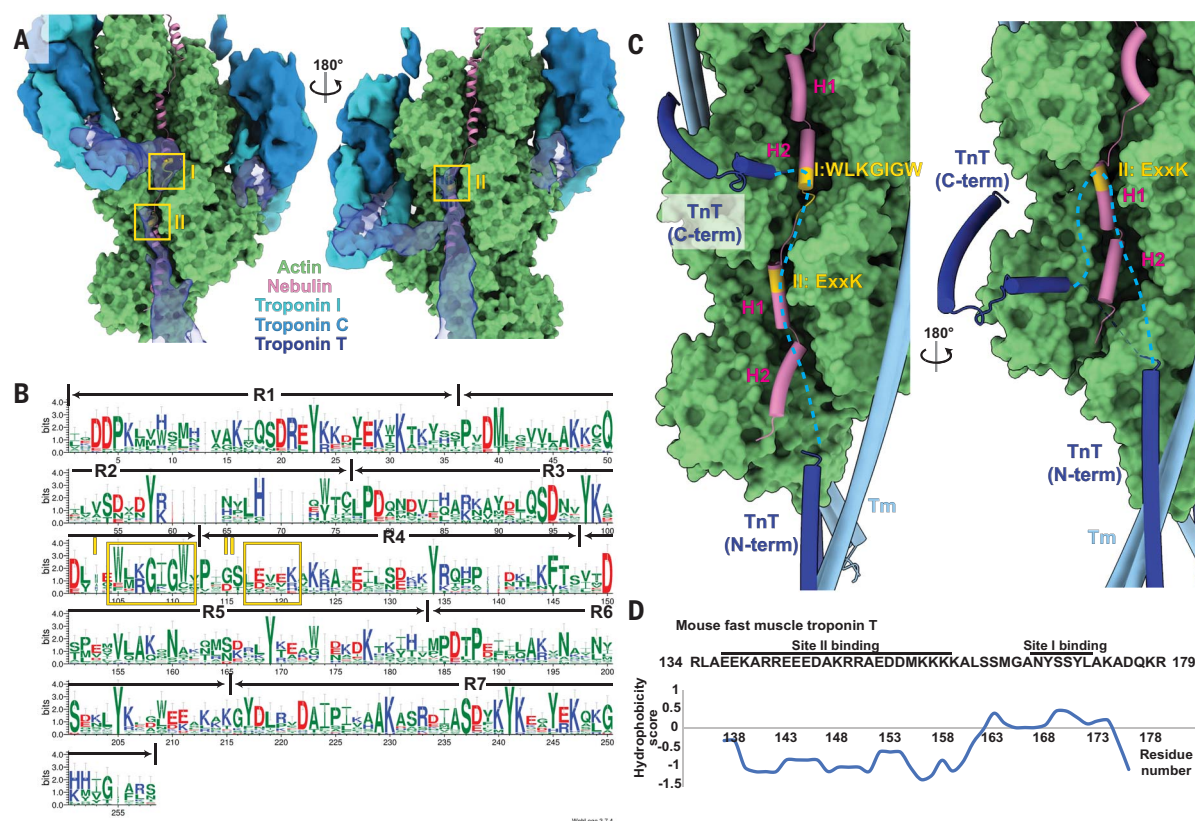


**Fig. 6. Potential interactions between nebulin and TnT.** (A) The actin-nebulin complex superimposed with the cryo-electron microscopy (cryo-EM) densities of the troponin complex (EMD-0729). Two contact sites between nebulin and TnT are marked in yellow as I and II. (B) Graphical representation of the sequence alignment of all nebulin super repeats (each super repeat contains the simple repeats R1 to R7). A larger amino acid symbol corresponds to a greater occurrence at a certain position. The troponin binding sites I and II are marked corresponding to the WLKGIGW and ExxK

motifs, respectively. (C) Two different TnT models (dark blue) that bind to opposite sides of the actin filament (PDB: 6KN8) are shown. The linker region between R134 and R179 (corresponding to R151 and S198 in the original model) is missing in the structural model. Possible shapes of the TnT linkers are marked as cyan dotted lines based on weak EM densities (EMD-0729). Potential TnT binding sites on nebulin are highlighted in yellow. Tropomyosin (Tm) is shown in light blue. (D) Hydrophobicity of the linker in mouse fast muscle TnT (TNNT3). Potential regions that can bind to sites I and II are marked.

acquisition. Tilt series of the skeletal A-band dataset were acquired at 81,000 $\times$  nominal magnification {pixel size, 1.73 Å; calibrated based on an averaged reconstruction and a crystal structure of myosin [Protein Data Bank (PDB) ID: 3I5G] (52)} with the K2 Summit camera. Tilt series of the cardiac A-band dataset and the skeletal I-band dataset were acquired with the K3 camera, at 42,000 $\times$  (pixel size, 2.23 Å) or 81,000 $\times$  (pixel size, 1.18 Å) nominal magnification, respectively. A dose-symmetric tilting scheme (53) was used during acquisition with a tilt range of  $-54^\circ$  to  $54^\circ$  relative to the lamella plane at  $3^\circ$  increments. A total dose of 130 to 150  $e^-/\text{Å}^2$  was applied to the sample.

#### Tomogram reconstruction and automatic filament picking

Individual tilt movies acquired from the microscope were motion corrected (54) and combined into stacks for a given tomogram with matched angles using a custom script for subsequent tomogram reconstruction. The combined stacks were then aligned, contrast transfer function (CTF) corrected through

strip-based phase flipping, and reconstructed using IMOD (55). In total, three datasets were collected: skeletal (psoas) A-band (171 tomograms), cardiac A-band (24 tomograms), and skeletal I-band (115 tomograms). Tomograms containing the wrong field of view, incompletely vitrified ice, or lacking visible inherent sarcomere features as a result of the lamella being too thick ( $>150$  nm) were discarded. Eventually, 48, 24, and 47 tomograms were selected from the skeletal A-band, cardiac A-band, and skeletal I-band datasets, respectively, for further processing.

#### Automated picking of the mouse psoas A-band

The picking of thin filaments within the mouse psoas A-band was performed as previously outlined (2). Briefly, tomograms were reoriented so that the thin and thick filaments of the sarcomere lay along the Y axis of the volume and such that XY slices contained the central section of the thin and thick filaments. After applying an equatorial filter as a Fourier mask, thin filaments were recognized and traced

from the XZ slices by the TrackMate plugin (56) in Fiji (57, 58). In total, 183,260 segments of the thin filaments (subtomograms) were picked from 48 tomograms with an intersegment distance of 62 Å. The distance was determined to accommodate two adjacent actin subunits on one strand for further averaging of myosin double head structure.

#### Automated picking of the mouse cardiac A-band

The picking of the mouse cardiac A-band thin filament used a similar approach as described above for skeletal A-band, with the following changes: After the rotation of the tomograms, from the XZ slices, positions of the thin filaments were determined using crYOLO (59) instead of TrackMate. Manual picking of thin filaments from 28 XZ slices from six tomograms were used for initial training in crYOLO. The positions for thin filament in all tomograms were then picked and traced by crYOLO. In total, 202,864 segments of the thin filaments were picked from 24 tomograms with an intersegment distance of 65 Å.



### *Automated picking of the mouse psoas I-band*

The picking of the mouse psoas I-band was performed using the latest development version of crYOLO (1.8.0b33) to pick directly on XY slices without any prerotation of tomograms. Tomograms were reconstructed using the program Warp after alignment in IMOD, at a down-sampled scale of 8×. Thin filaments were manually picked on 21 XY slices from four tomograms. These picked positions were then used to train a model in crYOLO, which was used to pick all tomograms. The picked positions were then traced through different XY planes in three dimensions. In total, 84,937 segments of I-band thin filaments were picked from 47 tomograms with an intersegment distance of 38 Å.

### *Subtomogram averaging*

#### *Skeletal A-band thin filament*

Subtomogram averaging of the skeletal A-band thin filaments first followed a previously published approach (2). Briefly, the determined positions for filaments within the tomograms were used to extract subtomograms in RELION (60) using a box size of 200 voxels (346 Å), which were then projected (central 100 slices) and sorted into good and bad particle classes through two-dimensional (2D) classification in ISAC (67). Good particles were then subjected to 3D refinement using a cylindrical reference in RELION, achieving a global resolution (0.143 criterion) of 8.8 Å.

To increase resolution, the particles were then subjected to further refinement in the program M (62). Tilt movies and image stacks were motion corrected and CTF-estimated within Warp (63) and new tomograms were reconstructed. The original particle position information obtained from the final step of refinement in RELION was then transformed to match the output geometry of tomograms from Warp. The new particles were extracted in Warp for subsequent averaging in RELION using a 2× down sampling. After 3D refinement in RELION, the structure of the thin filament was determined to 7.8 Å (fig. S1). The final half maps and alignment parameters were subjected to M for refinement. The strategy for refinement in M followed previously published regimens (62). After this refinement, the structure reached a global resolution of 6.7 Å. The core of the thin filament, including actin and nebulin, was masked and reached a resolution of 4.5 Å (figs. S1 and S2), which was used for model building of actin and nebulin.

#### *Skeletal A-band actomyosin and myosin neck domain*

To resolve the actomyosin structure, including thin filaments and a bound myosin double head, a 3D classification approach similar to

the one previously published (2) was used. After the refinement in M, subtomograms were re-extracted and classified in RELION. Classes were translated and rotated to a common double-head configuration and re-refined in M. The final reconstruction at a resolution of 6.6 Å was used for model building of the myosin heavy chain. To increase the resolution of the myosin neck domains [predominantly the essential light chain (ELC) and RLC], the subtomograms were first recentered toward the ELC and re-refined in RELION with a mask containing only myosin. This resulted in an ELC-centered myosin double-head structure with a resolution of 8.9 Å (fig. S1). Afterward, the subtomograms were further recentered toward the RLC and re-refined with a smaller mask containing ELCs and RLCs to reconstruct a structure of RLC-centered myosin double head with a resolution of 9 Å. The ELC- and RLC-centered myosin double-head maps were used for rigid-body docking of the ELC and RLC models, respectively.

#### *Cardiac A-band thin filament, actomyosin, and myosin neck domain*

Subtomogram averaging of the cardiac A-band thin filament followed the same strategy as that for the A-band of skeletal muscle and resulted in a structure of thin filament resolved to a global resolution of 8 Å, with the core of the thin filament (actin) resolved to 6.3 Å (fig. S3, A and B). Structures of cardiac actomyosin and myosin neck domain were determined using the same classification and recentering approach as that used for skeletal structures, resulting in resolutions of 7.7 and 12 Å, respectively.

#### *Skeletal I-band thin filament*

Subtomogram averaging of the skeletal I-band thin filament excluding troponin was performed largely as described for the A-band structures, except for using helical symmetry (twist −167.4°, rise 28.8 Å) during the initial refinement in RELION to reduce alignment error as a result of the missing wedge artifacts. The final structure of the I-band thin filament was determined to a global resolution of 9.4 Å, with the core (actin and nebulin) resolved to 7.4 Å (fig. S3, C and D). Subtomogram averaging of the thin filament including troponin was performed as previously described (2). A total of 2030 manually picked subtomograms were used for averaging using a cylinder-like reference generated from averaging all particles without alignment.

#### *Model building of actin, nebulin, and myosin heavy chain*

To reduce the risk of overrefinement and account for the heterogeneous resolution of our structures, several density maps—which were masked to different areas, filtered to nominal or local resolution as determined by

SPHIRE (64), and sharpened using various B-factors—were used for model building. In addition, density modified maps were calculated from half maps providing the reported nominal resolution (65).

An initial model for actin was generated by homology modeling using Modeller (66) in Chimera based on a previous atomic model [PDB: 5JLH (67), chain A] and a sequence alignment from Clustal Ω. The unresolved N terminus of actin (amino acids 1 to 6) was removed and Mg<sup>2+</sup>-adenosine 5'-diphosphate (ADP) was added from PDB 5LJH. HIS 73 was replaced by HIC (4-methyl-histidine) and regularized in Coot (68). A pentameric composite model was assembled by rigid-body fitting in Chimera including an initial model of nebulin (see below). Model building was performed in ISOLDE (69) in ChimeraX (70). A total of four density maps were loaded (filtered to nominal resolution and sharpened with B-factors −70 and −150, filtered to local resolution and sharpened to B-factor −100, and the density-modified map). Only the central actin chain and residues in close contact were included in the simulation and rebuilt. Unresolved side chains are in the most likely positions. After a first pass through the complete molecule, Ramachandran and rotamer issues were addressed locally. Based on the refined central chain, the composite actin-nebulin pentamer was updated. Hydrogens were removed, and the resulting model was real-space refined against the map filtered to nominal resolution in Phenix (71). To avoid large deviations from the input model, the ISOLDE model was used as a reference, while local grid search, rotamer, and Ramachandran restraints were deactivated. The actin model was further improved by a second round of model building in ISOLDE.

Modeling of nebulin was performed in analogy. An initial polyalanine model for nebulin was built manually in Coot based on the density of the central repeat (4.5-Å resolution). To cover the connection between two nebulin repeats, a peptide of 56 amino acids (instead of 35 amino acids) was initially built. The density corresponding to residue 22 was consistent with a consensus tyrosine residue, so tyrosine was used instead of alanine. A segmented postprocessed map (filtered to nominal resolution and sharpened with B-factor −70) was loaded for further modeling in ISOLDE. Secondary structure and rotamer restraints were applied where appropriate. Based on the resulting model, a continuous model of nebulin was created by first cutting the model to 35 amino acids and rigid-body fitting into the density. The termini of three consecutive nebulin chains were then manually connected. To address geometry issues caused by the connection, the combined nebulin chain was real-space refined in Phenix against the segmented

map and subjected to another round of refinement in ISOLDE.

Refined models of actin and nebulin were finally combined into one pentameric model. Minor adjustments to the orientation of side chains were done in Coot where necessary. The composite model was real-space refined against the 4.5-Å-resolution map filtered to local resolution (B-factor -100) in Phenix using the same settings as before.

An initial model of the actin-nebulin-tropomyosin-myosin (actomyosin) complex was assembled from the refined actin-nebulin model, a homology model of myosin (52) (PDB: 3I5G, chain A), and a polyalanine model of tropomyosin (67) (PDB: 5JLH, chains J and K) using rigid-body fitting. Only the heavy chain of myosin (up to residue 788) was modeled. After the addition of hydrogens, the central myosin chain was refined in ISOLDE using four segmented density maps of actomyosin, as described for actin. All applicable secondary structure restraints and many rotamer restraints were applied. Manual building was started from the acto-myosin interface, as it is best resolved. Unresolved residues including loop 1 (amino acids 207 to 215), loop 2 (626 to 643), and the N terminus (1 to 11) were removed. After deletion of hydrogens, the resulting atomic model was real-space refined in Phenix and further improved by a second round of refinement in ISOLDE. The refined atomic model of the central myosin chain was finally used to assemble an updated composite model of the actomyosin complex. This model was subjected to a final round of real-space refinement in Phenix against a 6.6-Å-resolution density map filtered to nominal resolution (B-factor -75) using the same settings as before, but with both Ramachandran and Rotamer restraints applied.

Because the resolution was not sufficient to reliably model  $Mg^{2+}$  ions, they were replaced with the ones from PDB 5JLH by superposition of actin subunits. The final atomic models of actin-nebulin and actomyosin complexes were assessed by Molprobit (72) and EMRinger (73) statistics (table S1).

#### Rigid-body docking of myosin light chains

Because the density for the C terminus of the myosin heavy chain lever arm as well as the ELC and RLC is of insufficient quality for reliable model building with refinement, rigid-body docking of previously published structural models (52) (PDB: 3I5G) was performed. First, the ELC model together with the ELC-binding lever arm helix (amino acids 785 to 802 in PDB 3I5G) were docked into both myosin ELC densities in the ELC-centered myosin double-head map (8.9 Å, B-factor -500) in Chimera. Then, the RLC model together with RLC-binding HC helices (amino acids 809 to 839) were docked into the RLC density of the leading myosin

head in the RLC-centered myosin double-head map (9 Å, B-factor -300). For the RLC of the trailing head, the C-lobe of RLC (together with HC helix amino acids 809 to 824) and the N-lobe of RLC (together with HC helix amino acids 826 to 839) were docked separately into a segmented map of trailing myosin RLC (fig. S5). The maps of actomyosin, ELC-centered myosin double head, and RLC-centered myosin double head were aligned in Chimera to unify the coordinate system of all models. In the end, a final homology model was calculated on the basis of these initial models and the sequences of mouse myosin heavy chain and light chains from mouse fast muscles using SWISS-MODEL (74). To compare the difference of the RLC-RLC interface between active and inactive myosin, this model was compared with previous structures of myosin IHM (38) (PDB: 6XE9) through aligning the leading head RLC from our model to the free head RLC from IHM in Chimera.

#### Sequence analysis of nebulin and TnT

Because a defined boundary on the nebulin sequence between the A-band and I-band is not present, the nebulin sequence of M1 to M8 and the entire super repeat region (Fig. 4A) from a mouse (Uniprot: E9Q1W3) was considered as the A-band nebulin sequence and divided into 176 simple repeats (M1 to M162) through placing the SDxxYK motif at positions 18 to 23. Multiple sequence alignment was performed using ClustalW (75) with gaps disabled (fig. S8A) and visualized in WebLogo (76). Secondary structure of each simple repeat was predicted using RaptorX-Property (77). Probability values for there being an  $\alpha$  helix at each residue position were averaged and used for Fig. 4 and fig. S8. To estimate relationship between the charge of the amino acid at position 15 and 21 a Bayesian multinomial regression was performed. For both positions and for each of the 176 sequences, the amino acid type was assigned a number, representing one of four categories: 1 (positive), 2 (negative), 3 (hydrophobic), or 4 (other). With this, the categorical variables  $y_{i,j}^{15}$  and  $y_{i,j}^{21}$  were constructed, representing the category  $i$  at positions 15 and 21 for sequence  $j$ , respectively. The hierarchical Bayesian model was then modeled in the following way and fitted with Stan (78)

$$\begin{aligned} \alpha_i &\sim \text{normal}(0, 1) \\ \beta_i &\sim \text{normal}(-0.3, 1.5) \\ y_{i,j}^{21} &= \text{softmax}\left(\alpha_i + \sum_{k=1}^4 \beta_k x_{i,j}^{15}\right) \\ p_{i,j}^{15} &= \text{cat}\left(y_{i,j}^{21}\right) \end{aligned}$$

Here,  $\alpha_i$  is the intercept,  $\beta_i$  is the regression coefficients, and  $p_{i,j}^{15}$  is the probability of seeing category  $i$  in sequence  $j$ . The variable  $x_{i,j}^{15}$  is

an indicator variable, which is 1 when sequence  $j$  at position 15 is of class  $i$ . The priors for  $\alpha_i$  and  $\beta_i$  were chosen in a way so that the prior predictive distribution of  $p_{i,j}^{15}$  has a mean probability for each class of 0.18. After fitting, 1000 samples were drawn from the posterior distribution for each possible state of category of amino acid 21 (fig. S9B).

TnT linker sequence was from mouse fast skeletal muscle TnT (UniProt: Q9QZ47-1) after sequence alignment with the sequence of the missing segment of TnT (R151 to S198) in PDB: 6KN8 (34). The hydrophobicity score (Fig. 6D) was calculated through ProtScale (79), using the scale from Abraham and Leo (80).

#### REFERENCES AND NOTES

- M. Yuen, C. A. C. Ottenheim, Nebulin: Big protein with big responsibilities. *J. Muscle Res. Cell Motil.* **41**, 103–124 (2020). doi: [10.1007/s10974-019-09565-3](https://doi.org/10.1007/s10974-019-09565-3); pmid: [31982973](https://pubmed.ncbi.nlm.nih.gov/31982973/)
- Z. Wang et al., The molecular basis for sarcomere organization in vertebrate skeletal muscle. *Cell* **184**, 2135–2150.e13 (2021). doi: [10.1016/j.cell.2021.02.047](https://doi.org/10.1016/j.cell.2021.02.047); pmid: [33765442](https://pubmed.ncbi.nlm.nih.gov/33765442/)
- K. Wang, C. L. Williamson, Identification of an N2 line protein of striated muscle. *Proc. Natl. Acad. Sci. U.S.A.* **77**, 3254–3258 (1980). doi: [10.1073/pnas.77.6.3254](https://doi.org/10.1073/pnas.77.6.3254); pmid: [6997874](https://pubmed.ncbi.nlm.nih.gov/6997874/)
- K. Wang, J. Wright, Architecture of the sarcomere matrix of skeletal muscle: Immunoelectron microscopic evidence that suggests a set of parallel inextensible nebulin filaments anchored at the Z line. *J. Cell Biol.* **107**, 2199–2212 (1988). doi: [10.1083/jcb.107.6.2199](https://doi.org/10.1083/jcb.107.6.2199); pmid: [3058720](https://pubmed.ncbi.nlm.nih.gov/3058720/)
- C. T. Pappas, P. A. Krieg, C. C. Gregorio, Nebulin regulates actin filament lengths by a stabilization mechanism. *J. Cell Biol.* **189**, 859–870 (2010). doi: [10.1083/jcb.201001043](https://doi.org/10.1083/jcb.201001043); pmid: [20498015](https://pubmed.ncbi.nlm.nih.gov/20498015/)
- N. B. Romero, S. A. Sandaradura, N. F. Clarke, Recent advances in nemaline myopathy. *Curr. Opin. Neurol.* **26**, 519–526 (2013). doi: [10.1097/WCO.0b013e328364d681](https://doi.org/10.1097/WCO.0b013e328364d681); pmid: [23995272](https://pubmed.ncbi.nlm.nih.gov/23995272/)
- C. A. Sewry, J. M. Lailla, C. Wallgren-Pettersson, Nemaline myopathies: A current view. *J. Muscle Res. Cell Motil.* **40**, 111–126 (2019). doi: [10.1007/s10974-019-09519-9](https://doi.org/10.1007/s10974-019-09519-9); pmid: [31228046](https://pubmed.ncbi.nlm.nih.gov/31228046/)
- M. M. Ryan et al., Nemaline myopathy: A clinical study of 143 cases. *Ann. Neurol.* **50**, 312–320 (2001). doi: [10.1002/ana.1080](https://doi.org/10.1002/ana.1080); pmid: [11558787](https://pubmed.ncbi.nlm.nih.gov/11558787/)
- C. L. Moncman, K. Wang, Nebulette: A 107 kD nebulin-like protein in cardiac muscle. *Cell Motil. Cytoskeleton* **32**, 205–225 (1995). doi: [10.1002/cm.970320305](https://doi.org/10.1002/cm.970320305); pmid: [8581976](https://pubmed.ncbi.nlm.nih.gov/8581976/)
- T. Burgoyne, F. Muhammad, P. K. Luther, Visualization of cardiac muscle thin filaments and measurement of their lengths by electron tomography. *Cardiovasc. Res.* **77**, 707–712 (2008). doi: [10.1093/cvr/cvm117](https://doi.org/10.1093/cvr/cvm117); pmid: [18178575](https://pubmed.ncbi.nlm.nih.gov/18178575/)
- J. Kolb et al., Thin filament length in the cardiac sarcomere varies with sarcomere length but is independent of titin and nebulin. *J. Mol. Cell. Cardiol.* **97**, 286–294 (2016). doi: [10.1016/j.yjmcc.2016.04.013](https://doi.org/10.1016/j.yjmcc.2016.04.013); pmid: [27139341](https://pubmed.ncbi.nlm.nih.gov/27139341/)
- S. Labeit, B. Kolmerer, The complete primary structure of human nebulin and its correlation to muscle structure. *J. Mol. Biol.* **248**, 308–315 (1995). doi: [10.1016/S0022-2836\(95\)80052-2](https://doi.org/10.1016/S0022-2836(95)80052-2); pmid: [7739042](https://pubmed.ncbi.nlm.nih.gov/7739042/)
- K. Donner, M. Sandbacka, V. L. Lehtokari, C. Wallgren-Pettersson, K. Pelin, Complete genomic structure of the human nebulin gene and identification of alternatively spliced transcripts. *Eur. J. Hum. Genet.* **12**, 744–751 (2004). doi: [10.1038/sj.ejhg.5201242](https://doi.org/10.1038/sj.ejhg.5201242); pmid: [15266303](https://pubmed.ncbi.nlm.nih.gov/15266303/)
- A. S. McElhinny, B. Kolmerer, V. M. Fowler, S. Labeit, C. C. Gregorio, The N-terminal end of nebulin interacts with tropomodulin at the pointed ends of the thin filaments. *J. Biol. Chem.* **276**, 583–592 (2001). doi: [10.1074/jbc.M005693200](https://doi.org/10.1074/jbc.M005693200); pmid: [11016930](https://pubmed.ncbi.nlm.nih.gov/11016930/)
- C. T. Pappas, N. Bhattacharya, J. A. Cooper, C. C. Gregorio, Nebulin interacts with CapZ and regulates thin filament architecture within the Z-disc. *Mol. Biol. Cell* **19**, 1837–1847 (2008). doi: [10.1091/mbc.e07-07-0690](https://doi.org/10.1091/mbc.e07-07-0690); pmid: [18272787](https://pubmed.ncbi.nlm.nih.gov/18272787/)
- S. Labeit et al., Evidence that nebulin is a protein-ruler in muscle thin filaments. *FEBS Lett.* **282**, 313–316 (1991). doi: [10.1016/0014-5793\(91\)80503-U](https://doi.org/10.1016/0014-5793(91)80503-U); pmid: [2037050](https://pubmed.ncbi.nlm.nih.gov/2037050/)
- D. S. Gokhin et al., Thin-filament length correlates with fiber type in human skeletal muscle. *Am. J. Physiol. Cell Physiol.*



302. C555–C565 (2012). doi: [10.1152/ajpcell.00299.2011](https://doi.org/10.1152/ajpcell.00299.2011); pmid: [22075691](https://pubmed.ncbi.nlm.nih.gov/22075691/)
18. B. Kiss *et al.*, Nebulin and Lmod2 are critical for specifying thin-filament length in skeletal muscle. *Sci. Adv.* **6**, eabc1992 (2020). doi: [10.1126/sciadv.abc1992](https://doi.org/10.1126/sciadv.abc1992); pmid: [33177085](https://pubmed.ncbi.nlm.nih.gov/33177085/)
19. V. M. Fowler, C. R. McKeown, R. S. Fischer, Nebulin: Does it measure up as a ruler? *Curr. Biol.* **16**, R18–R20 (2006). doi: [10.1016/j.cub.2005.12.003](https://doi.org/10.1016/j.cub.2005.12.003); pmid: [16401411](https://pubmed.ncbi.nlm.nih.gov/16401411/)
20. C. C. Witt *et al.*, Nebulin regulates thin filament length, contractility, and Z-disk structure *in vivo*. *EMBO J.* **25**, 3843–3855 (2006). doi: [10.1038/sj.emboj.7601242](https://doi.org/10.1038/sj.emboj.7601242); pmid: [16902413](https://pubmed.ncbi.nlm.nih.gov/16902413/)
21. M. L. Bang *et al.*, Nebulin-deficient mice exhibit shorter thin filament lengths and reduced contractile function in skeletal muscle. *J. Cell Biol.* **173**, 905–916 (2006). doi: [10.1083/jcb.200603119](https://doi.org/10.1083/jcb.200603119); pmid: [16769824](https://pubmed.ncbi.nlm.nih.gov/16769824/)
22. S. M. Gonsior, M. Gautel, H. Hinssen, A six-module human nebulin fragment bundles actin filaments and induces actin polymerization. *J. Muscle Res. Cell Motil.* **19**, 225–235 (1998). doi: [10.1023/A:1005372915268](https://doi.org/10.1023/A:1005372915268); pmid: [9583363](https://pubmed.ncbi.nlm.nih.gov/9583363/)
23. M. Pfuhl, S. J. Winder, A. Pastore, Nebulin, a helical actin binding protein. *EMBO J.* **13**, 1782–1789 (1994). doi: [10.1002/j.1460-2075.1994.tb06446.x](https://doi.org/10.1002/j.1460-2075.1994.tb06446.x); pmid: [8168478](https://pubmed.ncbi.nlm.nih.gov/8168478/)
24. S. Pospich, F. Merino, S. Raunser, Structural Effects and Functional Implications of Phalloidin and Jaspalakinolide Binding to Actin Filaments. *Structure* **28**, 437–449.e5 (2020). doi: [10.1016/j.str.2020.01.014](https://doi.org/10.1016/j.str.2020.01.014); pmid: [32084355](https://pubmed.ncbi.nlm.nih.gov/32084355/)
25. X. Ao, S. S. Lehrer, Phalloidin unzips nebulin from thin filaments in skeletal myofibrils. *J. Cell Sci.* **108**, 3397–3403 (1995). doi: [10.1242/jcs.108.11.3397](https://doi.org/10.1242/jcs.108.11.3397); pmid: [8586652](https://pubmed.ncbi.nlm.nih.gov/8586652/)
26. A. Castillo, R. Nowak, K. P. Littlefield, V. M. Fowler, R. S. Littlefield, A nebulin ruler does not dictate thin filament lengths. *Biophys. J.* **96**, 1856–1865 (2009). doi: [10.1016/j.bpj.2008.10.053](https://doi.org/10.1016/j.bpj.2008.10.053); pmid: [19254544](https://pubmed.ncbi.nlm.nih.gov/19254544/)
27. N. Lukoyanova *et al.*, Each actin subunit has three nebulin binding sites: Implications for steric blocking. *Curr. Biol.* **12**, 383–388 (2002). doi: [10.1016/S0960-9822\(02\)00678-4](https://doi.org/10.1016/S0960-9822(02)00678-4); pmid: [11882289](https://pubmed.ncbi.nlm.nih.gov/11882289/)
28. K. J. V. Poole *et al.*, A comparison of muscle thin filament models obtained from electron microscopy reconstructions and low-angle X-ray fibre diagrams from non-overlap muscle. *J. Struct. Biol.* **155**, 273–284 (2006). doi: [10.1016/j.jsb.2006.02.020](https://doi.org/10.1016/j.jsb.2006.02.020); pmid: [16793285](https://pubmed.ncbi.nlm.nih.gov/16793285/)
29. M. Marttila *et al.*, Nebulin interactions with actin and tropomyosin are altered by disease-causing mutations. *Skelet. Muscle* **4**, 15 (2014). doi: [10.1186/2044-5040-4-15](https://doi.org/10.1186/2044-5040-4-15); pmid: [25110572](https://pubmed.ncbi.nlm.nih.gov/25110572/)
30. J. Q. Zhang, A. Weisberg, R. Horowitz, Expression and purification of large nebulin fragments and their interaction with actin. *Biophys. J.* **74**, 349–359 (1998). doi: [10.1016/S0006-3495\(98\)77792-6](https://doi.org/10.1016/S0006-3495(98)77792-6); pmid: [9449335](https://pubmed.ncbi.nlm.nih.gov/9449335/)
31. R. Chitose *et al.*, Isolation of nebulin from rabbit skeletal muscle and its interaction with actin. *J. Biomed. Biotechnol.* **2010**, 108495 (2010). doi: [10.1155/2010/108495](https://doi.org/10.1155/2010/108495); pmid: [20467585](https://pubmed.ncbi.nlm.nih.gov/20467585/)
32. J. Jumper *et al.*, Highly accurate protein structure prediction with AlphaFold. *Nature* **596**, 583–589 (2021). doi: [10.1038/s41586-021-03819-2](https://doi.org/10.1038/s41586-021-03819-2); pmid: [34265844](https://pubmed.ncbi.nlm.nih.gov/34265844/)
33. M.-L. Bang *et al.*, Nebulin plays a direct role in promoting strong actin-myosin interactions. *FASEB J.* **23**, 4117–4125 (2009). doi: [10.1096/fj.09-137729](https://doi.org/10.1096/fj.09-137729); pmid: [19679637](https://pubmed.ncbi.nlm.nih.gov/19679637/)
34. M. Chandra *et al.*, Nebulin alters cross-bridge cycling kinetics and increases thin filament activation: A novel mechanism for increasing tension and reducing tension cost. *J. Biol. Chem.* **284**, 30889–30896 (2009). doi: [10.1074/jbc.M109.049718](https://doi.org/10.1074/jbc.M109.049718); pmid: [19736309](https://pubmed.ncbi.nlm.nih.gov/19736309/)
35. B. Kiss *et al.*, Nebulin stiffens the thin filament and augments cross-bridge interaction in skeletal muscle. *Proc. Natl. Acad. Sci. U.S.A.* **115**, 10369–10374 (2018). doi: [10.1073/pnas.1804726115](https://doi.org/10.1073/pnas.1804726115); pmid: [30249654](https://pubmed.ncbi.nlm.nih.gov/30249654/)
36. J. P. Jin, K. Wang, Cloning, expression, and protein interaction of human nebulin fragments composed of varying numbers of sequence modules. *J. Biol. Chem.* **266**, 21215–21223 (1991). doi: [10.1016/S0021-9258\(18\)54843-2](https://doi.org/10.1016/S0021-9258(18)54843-2); pmid: [1682316](https://pubmed.ncbi.nlm.nih.gov/1682316/)
37. D. D. Root, K. Wang, Calmodulin-sensitive interaction of human nebulin fragments with actin and myosin. *Biochemistry* **33**, 12581–12591 (1994). doi: [10.1021/bi00208a008](https://doi.org/10.1021/bi00208a008); pmid: [7918483](https://pubmed.ncbi.nlm.nih.gov/7918483/)
38. S. Yang *et al.*, Cryo-EM structure of the inhibited (10S) form of myosin II. *Nature* **588**, 521–525 (2020). doi: [10.1038/s41586-020-3007-0](https://doi.org/10.1038/s41586-020-3007-0); pmid: [33268893](https://pubmed.ncbi.nlm.nih.gov/33268893/)
39. C. A. Scarff *et al.*, Structure of the shutdown state of myosin-2. *Nature* **588**, 515–520 (2020). doi: [10.1038/s41586-020-2990-5](https://doi.org/10.1038/s41586-020-2990-5); pmid: [33268888](https://pubmed.ncbi.nlm.nih.gov/33268888/)
40. M. Kruger, J. Wright, K. Wang, Nebulin as a length regulator of thin filaments of vertebrate skeletal muscles: Correlation of thin filament length, nebulin size, and epitope profile. *J. Cell Biol.* **115**, 97–107 (1991). doi: [10.1083/jcb.115.1.97](https://doi.org/10.1083/jcb.115.1.97); pmid: [1717482](https://pubmed.ncbi.nlm.nih.gov/1717482/)
41. E. P. Manning, J. C. Tardiff, S. D. Schwartz, A model of calcium activation of the cardiac thin filament. *Biochemistry* **50**, 7405–7413 (2011). doi: [10.1021/bi200506k](https://doi.org/10.1021/bi200506k); pmid: [21797264](https://pubmed.ncbi.nlm.nih.gov/21797264/)
42. Y. Yamada, K. Namba, T. Fujii, Cardiac muscle thin filament structures reveal calcium regulatory mechanism. *Nat. Commun.* **11**, 153 (2020). doi: [10.1038/s41467-019-14008-1](https://doi.org/10.1038/s41467-019-14008-1); pmid: [31919429](https://pubmed.ncbi.nlm.nih.gov/31919429/)
43. C. M. Risi *et al.*, The structure of the native cardiac thin filament at systolic Ca<sup>2+</sup> levels. *Proc. Natl. Acad. Sci. U.S.A.* **118**, e2024288118 (2021). doi: [10.1073/pnas.2024288118](https://doi.org/10.1073/pnas.2024288118); pmid: [33735306](https://pubmed.ncbi.nlm.nih.gov/33735306/)
44. J. J. Johnston *et al.*, A novel nemaline myopathy in the Amish caused by a mutation in troponin T1. *Am. J. Hum. Genet.* **67**, 814–821 (2000). doi: [10.1086/303089](https://doi.org/10.1086/303089); pmid: [10952871](https://pubmed.ncbi.nlm.nih.gov/10952871/)
45. S. A. Sandaradura *et al.*, Nemaline myopathy and distal arthropropoglysis associated with an autosomal recessive *TNNI3* splice variant. *Hum. Mutat.* **39**, 383–388 (2018). doi: [10.1002/humu.23385](https://doi.org/10.1002/humu.23385); pmid: [2966598](https://pubmed.ncbi.nlm.nih.gov/2966598/)
46. S. T. Kazmierski *et al.*, The complete mouse nebulin gene sequence and the identification of cardiac nebulin. *J. Mol. Biol.* **328**, 835–846 (2003). doi: [10.1016/S0022-2836\(03\)00348-6](https://doi.org/10.1016/S0022-2836(03)00348-6); pmid: [12729758](https://pubmed.ncbi.nlm.nih.gov/12729758/)
47. V. L. Lehtokari *et al.*, Mutation update: The spectra of nebulin variants and associated myopathies. *Hum. Mutat.* **35**, 1418–1426 (2014). doi: [10.1002/humu.22693](https://doi.org/10.1002/humu.22693); pmid: [25205138](https://pubmed.ncbi.nlm.nih.gov/25205138/)
48. F. J. O'Reilly *et al.*, In-cell architecture of an actively transcribing-translating expressome. *Science* **369**, 554–557 (2020). doi: [10.1126/science.abb3758](https://doi.org/10.1126/science.abb3758); pmid: [32732422](https://pubmed.ncbi.nlm.nih.gov/32732422/)
49. R. J. Solaro, D. C. Pang, F. N. Briggs, The purification of cardiac myofibrils with Triton X-100. *Biochim. Biophys. Acta Bioenerg.* **245**, 259–262 (1971). doi: [10.1016/0005-2728\(71\)90033-8](https://doi.org/10.1016/0005-2728(71)90033-8); pmid: [4332100](https://pubmed.ncbi.nlm.nih.gov/4332100/)
50. S. Tacke *et al.*, A streamlined workflow for automated cryo focused ion beam milling. *J. Struct. Biol.* **213**, 107743 (2021). doi: [10.1016/j.jsb.2021.107743](https://doi.org/10.1016/j.jsb.2021.107743); pmid: [33971286](https://pubmed.ncbi.nlm.nih.gov/33971286/)
51. D. N. Mastronarde, Automated electron microscope tomography using robust prediction of specimen movements. *J. Struct. Biol.* **152**, 36–51 (2005). doi: [10.1016/j.jsb.2005.07.007](https://doi.org/10.1016/j.jsb.2005.07.007); pmid: [16182563](https://pubmed.ncbi.nlm.nih.gov/16182563/)
52. Y. Yang *et al.*, Rigor-like structures from muscle myosins reveal key mechanical elements in the transduction pathways of this allosteric motor. *Structure* **15**, 553–564 (2007). doi: [10.1016/j.str.2007.03.010](https://doi.org/10.1016/j.str.2007.03.010); pmid: [17502101](https://pubmed.ncbi.nlm.nih.gov/17502101/)
53. W. J. H. Hagen, W. Wan, J. A. G. Briggs, Implementation of a cryo-electron tomography tilt-scheme optimized for high resolution subtomogram averaging. *J. Struct. Biol.* **197**, 191–198 (2017). doi: [10.1016/j.jsb.2016.06.007](https://doi.org/10.1016/j.jsb.2016.06.007); pmid: [27131000](https://pubmed.ncbi.nlm.nih.gov/27131000/)
54. S. Q. Zheng *et al.*, MotionCor2: Anisotropic correction of beam-induced motion for improved cryo-electron microscopy. *Nat. Methods* **14**, 331–332 (2017). doi: [10.1038/nmeth.4193](https://doi.org/10.1038/nmeth.4193); pmid: [28250466](https://pubmed.ncbi.nlm.nih.gov/28250466/)
55. J. R. Kremer, D. N. Mastronarde, J. R. McIntosh, Computer visualization of three-dimensional image data using IMOD. *J. Struct. Biol.* **116**, 71–76 (1996). doi: [10.1006/jsbi.1996.0013](https://doi.org/10.1006/jsbi.1996.0013); pmid: [8742726](https://pubmed.ncbi.nlm.nih.gov/8742726/)
56. J. Y. Tinevez *et al.*, TrackMate: An open and extensible platform for single-particle tracking. *Methods* **115**, 80–90 (2017). doi: [10.1016/j.jmeth.2016.09.016](https://doi.org/10.1016/j.jmeth.2016.09.016); pmid: [27713081](https://pubmed.ncbi.nlm.nih.gov/27713081/)
57. J. Schindelin *et al.*, Fiji: An open-source platform for biological-image analysis. *Nat. Methods* **9**, 676–682 (2012). doi: [10.1038/nmeth.2019](https://doi.org/10.1038/nmeth.2019); pmid: [22743772](https://pubmed.ncbi.nlm.nih.gov/22743772/)
58. C. A. Schneider, W. S. Rasband, K. W. Eliceiri, NIH Image to ImageJ: 25 years of image analysis. *Nat. Methods* **9**, 671–675 (2012). doi: [10.1038/nmeth.2089](https://doi.org/10.1038/nmeth.2089); pmid: [22930834](https://pubmed.ncbi.nlm.nih.gov/22930834/)
59. T. Wagner *et al.*, SPHIRE-crYOLO is a fast and accurate fully automated particle picker for cryo-EM. *Commun. Biol.* **2**, 218 (2019). doi: [10.1038/s42003-019-0437-z](https://doi.org/10.1038/s42003-019-0437-z); pmid: [31240256](https://pubmed.ncbi.nlm.nih.gov/31240256/)
60. T. A. M. Bharat, S. H. W. Scheres, Resolving macromolecular structures from electron cryo-tomography data using subtomogram averaging in RELION. *Nat. Protoc.* **11**, 2054–2065 (2016). doi: [10.1038/nprot.2016.124](https://doi.org/10.1038/nprot.2016.124); pmid: [27685097](https://pubmed.ncbi.nlm.nih.gov/27685097/)
61. Z. Yang, J. Fang, J. Chittuluru, F. J. Asturias, P. A. Penczek, Iterative stable alignment and clustering of 2D transmission electron microscope images. *Structure* **20**, 237–247 (2012). doi: [10.1016/j.str.2011.12.007](https://doi.org/10.1016/j.str.2011.12.007); pmid: [22325773](https://pubmed.ncbi.nlm.nih.gov/22325773/)
62. D. Tegunov, L. Xue, C. Dienemann, P. Cramer, J. Mahamid, Multi-particle cryo-EM refinement with M visualizes ribosome-antibiotic complex at 3.5 Å in cells. *Nat. Methods* **18**, 186–193 (2021). doi: [10.1038/s41592-020-01054-7](https://doi.org/10.1038/s41592-020-01054-7); pmid: [33542511](https://pubmed.ncbi.nlm.nih.gov/33542511/)
63. D. Tegunov, P. Cramer, Real-time cryo-electron microscopy data preprocessing with Warp. *Nat. Methods* **16**, 1146–1152 (2019). doi: [10.1038/s41592-019-0580-y](https://doi.org/10.1038/s41592-019-0580-y); pmid: [31591575](https://pubmed.ncbi.nlm.nih.gov/31591575/)
64. T. Moriya *et al.*, High-resolution single particle analysis from electron cryo-microscopy images using SPHIRE. *J. Vis. Exp.* **123**, e55448 (2017). doi: [10.3791/55448](https://doi.org/10.3791/55448); pmid: [28570515](https://pubmed.ncbi.nlm.nih.gov/28570515/)
65. T. C. Terwilliger, S. J. Ludtke, R. J. Read, P. D. Adams, P. V. Afonine, Improvement of cryo-EM maps by density modification. *Nat. Methods* **17**, 923–927 (2020). doi: [10.1038/s41592-020-0914-9](https://doi.org/10.1038/s41592-020-0914-9); pmid: [32807957](https://pubmed.ncbi.nlm.nih.gov/32807957/)
66. N. Eswar, D. Eramian, B. Webb, M.-Y. Shen, A. Sali, in *Structural Proteomics: High-Throughput Methods*, B. Kobe, M. Guss, T. Huber, Eds., vol. 426 of *Methods in Molecular Biology* (Humana Press, 2008), pp. 145–159. doi: [10.1007/978-1-60327-058-8\\_8](https://doi.org/10.1007/978-1-60327-058-8_8)
67. J. von der Ecken, S. M. Heissler, S. Pathan-Chhatbar, D. J. Manstein, S. Raunser, Cryo-EM structure of a human cytoplasmic actomyosin complex at near-atomic resolution. *Nature* **534**, 724–728 (2016). doi: [10.1038/nature18295](https://doi.org/10.1038/nature18295); pmid: [27324845](https://pubmed.ncbi.nlm.nih.gov/27324845/)
68. P. Emsley, B. Lohkamp, W. G. Scott, K. Cowtan, Features and development of Coot. *Acta Cryst. D66*, 486–501 (2010). doi: [10.1107/S0907444910007493](https://doi.org/10.1107/S0907444910007493); pmid: [20383002](https://pubmed.ncbi.nlm.nih.gov/20383002/)
69. T. I. Croll, *ISOLDE*: A physically realistic environment for model building into low-resolution electron-density maps. *Acta Cryst. D74*, 519–530 (2018). doi: [10.1107/S2059798318002425](https://doi.org/10.1107/S2059798318002425); pmid: [29872003](https://pubmed.ncbi.nlm.nih.gov/29872003/)
70. T. D. Goddard *et al.*, UCSF ChimeraX: Meeting modern challenges in visualization and analysis. *Protein Sci.* **27**, 14–25 (2018). doi: [10.1002/pro.3235](https://doi.org/10.1002/pro.3235); pmid: [28710774](https://pubmed.ncbi.nlm.nih.gov/28710774/)
71. P. V. Afonine *et al.*, New tools for the analysis and validation of cryo-EM maps and atomic models. *Acta Cryst. D74*, 814–840 (2018). doi: [10.1107/S2059798318009324](https://doi.org/10.1107/S2059798318009324); pmid: [30198894](https://pubmed.ncbi.nlm.nih.gov/30198894/)
72. V. B. Chen *et al.*, MolProbity: All-atom structure validation for macromolecular crystallography. *Acta Cryst. D66*, 12–21 (2010). doi: [10.1107/S0907444909042073](https://doi.org/10.1107/S0907444909042073); pmid: [20057044](https://pubmed.ncbi.nlm.nih.gov/20057044/)
73. B. A. Barad *et al.*, EMRinger: Side chain-directed model and map validation for 3D cryo-electron microscopy. *Nat. Methods* **12**, 943–946 (2015). doi: [10.1038/nmeth.3541](https://doi.org/10.1038/nmeth.3541); pmid: [26280328](https://pubmed.ncbi.nlm.nih.gov/26280328/)
74. A. Waterhouse *et al.*, SWISS-MODEL: Homology modelling of protein structures and complexes. *Nucleic Acids Res.* **46**, W296–W303 (2018). doi: [10.1093/nar/gky427](https://doi.org/10.1093/nar/gky427); pmid: [29788355](https://pubmed.ncbi.nlm.nih.gov/29788355/)
75. M. A. Larkin *et al.*, Clustal W and Clustal X version 2.0. *Bioinformatics* **23**, 2947–2948 (2007). doi: [10.1093/bioinformatics/btm404](https://doi.org/10.1093/bioinformatics/btm404); pmid: [17846036](https://pubmed.ncbi.nlm.nih.gov/17846036/)
76. G. E. Crooks, G. Hon, J. M. Chandonia, S. E. Brenner, WebLogo: A sequence logo generator. *Genome Res.* **14**, 1188–1190 (2004). doi: [10.1101/gr.849004](https://doi.org/10.1101/gr.849004); pmid: [15173120](https://pubmed.ncbi.nlm.nih.gov/15173120/)
77. S. Wang, W. Li, S. Liu, J. Xu, RaptorX-Property: A web server for protein structure property prediction. *Nucleic Acids Res.* **44**, W430–W435 (2016). doi: [10.1093/nar/gkw306](https://doi.org/10.1093/nar/gkw306); pmid: [27112573](https://pubmed.ncbi.nlm.nih.gov/27112573/)
78. Stan Development Team, Stan Modeling Language Users Guide and Reference Manual, version 2.27 (2019); <https://mc-stan.org>
79. E. Gasteiger, C. Hoogland, A. Gattiker, S. Duvaud, M. R. Wilkins, R. D. Appel, A. Bairoch, in *The Proteomics Protocols Handbook*, J. M. Walker, Ed. (Humana Press, 2005), pp. 571–607. doi: [10.1385/1-59259-890-0-571](https://doi.org/10.1385/1-59259-890-0-571)
80. D. J. Abraham, A. J. Leo, Extension of the fragment method to calculate amino acid zwitterion and side chain partition coefficients. *Proteins* **2**, 130–152 (1987). doi: [10.1002/prot.340020207](https://doi.org/10.1002/prot.340020207); pmid: [3447171](https://pubmed.ncbi.nlm.nih.gov/3447171/)

## ACKNOWLEDGMENTS

We thank S. Tacke for hardware optimization for cryo-FIB milling. We are grateful to O. Hofnagel and D. Prumbaum for EM support and B. Brandmeier for technical support. We thank S. Biswas for support in manual particle selection. **Funding:** This work was supported by funds from the Max Planck Society (to S.R.), the Wellcome Trust (Collaborative Award in Sciences 201543/2/16/Z to S.R. and M.Ga.), the European Research Council under the European Union's Horizon 2020 Programme (ERC-2019-SyG, grant no. 856118 to S.R. and M.Ga.), and the Medical Research Council (MR/R003106/1 to M.Ga. and A.L.K.). M.Gr. was supported by an EMBO Long-Term Fellowship. M.Ga. holds the BHF Chair of Molecular Cardiology. **Author contributions:** S.R. designed and supervised the project. A.L.K. and M.Ga. developed methods and isolated mouse myofibrils. Z.W. performed cryo-FIB milling and collected cryo-ET data. M.Gr. optimized cryo-ET data acquisition. Z.W. and M.Gr. performed subtomogram averaging.

T.W. implemented automatic filament picking and tools for data conversion and statistical analysis. S.P. built atomic models for actin, nebulin, and myosin motor domain. Z.W. performed rigid-body fitting of myosin neck domain models. Z.W. prepared figures with the assistance of M.Gr. Z.W., M.Gr., M.Ga., and S.R. wrote the manuscript. All authors reviewed the results and commented on the manuscript. **Competing interests:** The authors declare no competing interests. **Data and materials availability:** Cryo-ET structures are deposited in the Electron Microscopy Data Bank under accession numbers EMD-13990 (skeletal A-band actin-nebulin), EMD-13991 (skeletal actomyosin), EMD-13992 (skeletal

ELC-centered myosin), EMD-13993 (skeletal RLC-centered myosin), EMD-13994 (skeletal I-band actin-nebulin), EMD-13995 (cardiac actin), EMD-13996 (cardiac actomyosin), and EMD-13997 (cardiac myosin neck domain). Representative tomograms are deposited under accession numbers EMD-13998 (skeletal A-band), EMD-13999 (skeletal I-band), and EMD-14000 (cardiac A-band). The atomic models are deposited in the Protein Data Bank under accession numbers 7QIM (skeletal actin-nebulin), 7QIN (skeletal actomyosin), and 7QIO (skeletal myosin neck domain). Other structures and EM density maps used in this study are available under PDB 3I5G, 6KN8, and 6XE9 and EMD-0729.

#### SUPPLEMENTARY MATERIALS

[science.org/doi/10.1126/science.abn1934](https://doi.org/10.1126/science.abn1934)

Figs. S1 to S11

Table S1

MDAR Reproducibility Checklist

Movies S1 to S4

[View/request a protocol for this paper from Bio-protocol.](#)

9 November 2021; accepted 12 January 2022

10.1126/science.abn1934